The development and comparison of endmember extraction algorithms using hyperspectral imagery

LI Ersen[1,2], ZHU Shulong[1], ZHOU Xiaoming[1], YU Wenjie[1]

1. *Institute of Surveying and Mapping,Information Engineering University*, *Henan Zhengzhou* 450052, *China*;

2. *Key Laboratory of Mine Spatial Information Technologies*, *Henan Jiaozuo* 454000, *China*

Abstract: The mixels in the hypersepctral images not only influence the accuracy of target detection and classification, but also greatly hinder the development of quantitative remote sensing. The typical endmember extraction algorithms now available are analyzed and summarized. These algorithms can be classified into two types based on the hypothesis of the existence of the pure pixels: endmember identification algorithm and endmember generation algorithm. Six endmember extraction algorithms, including N-FINDR, VCA, SGA, OSP, ICE and MVC-NMF, are introduced and compared using experimental data, which further show their advantages and disadvantages. With results of various methods, the future perspective is proposed for further study.

Key words: hyperspectral image, mixel, linear spectral mixing model, endmember

CLC number: TP79　　**Document code:** A

1 INTRODUCTION

The mixels exist abroadly in the hyperspectral images, and the mixed pixel decomposition is the effective approach to solve this problem to realize the sub-pixel classification (Kumar, *et al.*, 2008). The Linear Spectral Mixture Model (LSMM) is one of the Mixel Decomposition Model(MPD) that been applied most thoroughly and extensively. Its main procedure includes Dimension Reduction(DR), Endmember Extraction(EE) and Abundance Estimation(AE), in which the EE is the linchpin for the MPD. Based on the hypothesis of the existence of the pure pixels, the Endmember Extraction Algorithms(EEAs) can be categorized into two classes(Plaza, *et al.*, 2005) and they are Endmember Identification Algorithm(EIA) and Endmember Generation Algorithm(EGA). The EIA extracts pure pixels directly from the data. It is based on the pure pixel hypothesis and its theory is relatively simple while the EGA, on the other hand, generates the endmembers from the spectral data. For the hypserspectral data, pure pixels are rare due to the constraint of spatial resolution. Therefore, the precision of endmembers extracted by the EGA is often higher in the perspective of theory analysis.

The EIAs based on the LSMM mainly include Pixel Purity Index(PPI)(Boardman, *et al.*, 1995), N-FINDR (Winter, 1999a, 1999b, 2004), Sequential Maximum Angle Convex Cone(SMACC)

(Gruninger, *et al.*, 2004), Vertex Component Analysis(VCA) (Nascimento, *et al.*, 2005; Nascimento, 2006), Simplex Growing Algorithm(SGA) (Chang, *et al.*, 2006), Orthogonal Subspace Projection(OSP) (Harsanyi & Chang, 1994), and the Sequential Projection Algorithm(SPA)(Zhang, *et al.*, 2008). The EGAs mainly include Minimum Volume Transform(MVT)(Craig, *et al.*, 1994), Convex Cone Analysis(CCA)(Ifarraguerri & Chang, 1999), Iterative Error Analysi(IEA)(Neville, *et al.*, 1999), ORASIS(Bowles, *et al.*, 1995), Iterated Constrained Endmember(ICE)(Berman, *et al.*, 2003, 2004), and the Minimum Volume Constraint Nonnegative Matrix Factorization(MVC-NMF)(Miao, *et al.*, 2007). In this study, the four EIAs(N-FINDR, VCA, SGA, OSP) and two EGAs(ICE, MVC-NMF) are analyzed and compared for precision of the extracted endmembers and the efficiency of the algorithms using the experimental data These analysis and conclusions will build up bases for the further research, and can provide references for the other researchers.

2 ENDMEMBER IDENTIFICATION ALGORITHM

The LSMM assumes that the spectral response in each pixel is a linear combination of endmember spectras, with the weights being proportions. Let x denotes the l vector for one pixel in the image, l is the number of the bands, the mathematical formulation

---

of LSMM is

$$x = \sum_{i=1}^{p} A_i s_i + \varepsilon = As + \varepsilon \qquad (1)$$

where p is the number of the endmembers, A is the endmember matrix or source matrix, s is the abundance vector for the pixel, A_i and s_i is the ith endmember and mixing proportion, respectively, and ε represents the error term. Fig.1 is the sketch map for the LSMM. There are two constraints for the abundance vector in the LSMM: Abundance Non-negativity Constraint(ANC, $s_i \geqslant 0$, $i=1$, $2\cdots$, p) and Abundance Sum-to-one Constraint(ASC, $\sum_{i=1}^{p} s_i = 1$).
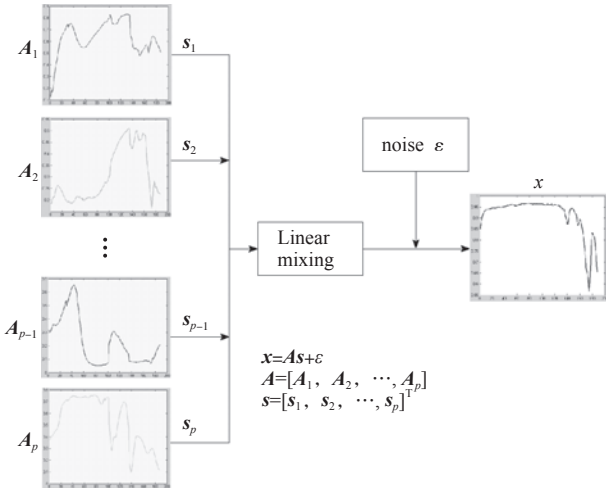

Fig. 1   The sketch map of LSMM

2.1   N-FINDR

N-FINDR algorithm searches the pure pixel set in the data based on the convex geometry. Its main theory can be described as follows. In the n-dimensional space, the simplex volume composed of the pure pixels is larger than any other ones composed of any other pixels, which is illustrated in the Fig.2. The algorithm finds the set of pixels with the largest possible volume by "inflating" a simplex inside the data, and it begins with a random set of vectors, in order to refine the estimates of the endmembers. Every pixel in the image must be evaluated as to its likelihood of being a pure or nearly pure pixel. To achieve this, the volume must be calculated with each pixel in a place of each endmember. A trial volume is calculated for every pixel in each endmember position by replacing that endmember and finding the volume. If the replacement results in an increase in volume, the pixel then replaces the endmember. This procedure is repeated until there are no more replacements of endmembers. Winter(1999a, 1999b) used this algorithm to extract endmembers successfully for the synthetic data, and justified that the N-FINDR is robust for the imperfect data. These results are demonstrated by the endmembers extracted from the AVIRIS Cuprite data set being similar with the reference data, and the abundance maps being consistent with the published mineral maps. Winter(2004) explained the N-FINDR algorithm extensively, and proved the validity of the algorithm from the theory analysis. Their analysis further justified that the algorithm could also converge the imperfect data.

The main procedures of the N-FINDR algorithm are as follows:

(1)Estimate or assign the number of endmembers p within the image data, and use the MNF(Minimum Noise Fraction) to reduce
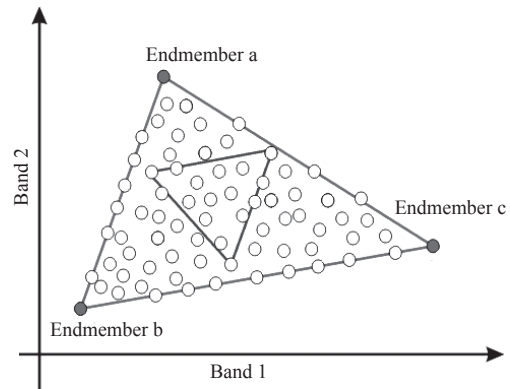

Fig. 2   Simplex and the endmember positions in the 2-D feature space

the dimensionality to be $p-1$.

(2)Select the pixels randomly as the initial endmembers, and calculate the simplex volume V_1 that composed of these initial endmembers. The mathematical definition of the volume of a simplex formed by the set of endmember estimates is

$$V(E) = \frac{1}{(p-1)!} \text{abs}(|E|) \qquad (2)$$

$$E = \begin{bmatrix} 1 & 1 & \cdots & 1 \\ A_1 & A_2 & \cdots & A_P \end{bmatrix} \qquad (3)$$

where A_i is the $p-1$ dimensional column vector for the ith endmember.

(3)Evaluate an image pixel by replacing one pixel in the represent endmember set with the image pixel P_1, producing a "trial enemember" set and calculate the new simplex volume V_2. If $V_2 > V_1$, replace the candidate enemember with P_1.

(4)Replace the other candidate enemembers with the pixel P, and execute the same procedure as (3).

(5)Execute the procedures (3) and (4) for all the other pixels repeatedly The simplex volume composed of the result endmembers is the largest one, and its vertexes correspond to the endmembers.

Winter(1999a, 1999b) indicated that N-FINDR will encounter difficulties in certain circumstances. It is feasible for a real image to contain no pure or nearly pure pixels. In this case, one of the basic assumptions of the algorithms has been violated. It finds the least mixed pixel that most closely approximates the endmember. Furthermore, if there are mixed pixels with a higher brightness than the unmixed pixels, the algorithm will select them as endmembers.

There are some shortcomings for the N-FINDR algorithm: (1)it does not have the rule or algorithm to estimate the number of endmembers; (2)it uses the random selection of vectors within the data to be the initial endmember set, which may result in time consuming iterations; (3)because of the random selection of endmembers, its endmember extraction results are always not repeatable; (4) it needs dimensionality reduction procedure, that can lead to errors. Furthermore, different dimensionality reduction algorithms will result in different endmember extraction results. Plaza(2005) used the VD method to estimate the number of endmembers, and initialized the endmember set with the IEA results. Results indicate that it can accelerate the algorithm' convergence and contribute to more stable results. Plaza and Chang(2006) studied the impact of the initialization methods(ATGP(Automatic Target Generation

Process), UFCLS(Unsupervised Fully Constrained Least Squares), IEA(Iterative Error Analysis), Maximin-Distance Algorithm) for the N-FINDR results, the experiments validated that the use of the initialization methods can both speed up the convergence and make some initial endmember in the ultimate endmember extraction results. Within the initialization methods, the ATGP can get the best results. A recent study (Zhang, *et al.*, 2009) that used the ATGP algorithm to initialize the N-FINDR, and replaced the volume calculation with the distance one, also indicated these improvements can speed up the algorithm's convergence.

2.2   VCA algorithm

VCA algorithm extracts the endmembers based on the convex geometry theory under the assumption of the pure pixel's existence. It considers the variations due to the surface topography, and models the data using a positive cone, whose projection onto a properly chosen hyperplane is a simplex with vertices being the endmembers. After projecting the data onto the selected hyperplane, VCA projects all image pixels to a random direction and uses the pixel with the largest projection as the first endmember. The other endmembers are identified by iteratively projecting data onto a direction orthogonal to the subspace spanned by the endmembers already determined. The new endmember is then selected as the pixel corresponding to the extreme projection.

Assuming the linear mixing scenario, each pixel vector is given by

$$x = A\gamma s + \varepsilon \qquad (4)$$

where γ is a scale factor modeling the illuminationvariability due to surface topography. Owning to physical constraints of abundance vector, $s \in \Delta_p$, Δ_p is a simplex. Each pixel can be viewed as a vector in an l-dimensional Euclidean space, where each channel is assigned to one axis of space. $S_x = \left\{ x \in R^l : x = As, s \in \Delta_p \right\}$ is also a simplex. $C_p = \left\{ x \in R^l : x = A\gamma s, s \in \Delta_p, \gamma \geqslant 0 \right\}$ is a conex cone, owing to the scale factor γ.

The projective projection of convex cone C_p onto a properly chosen hyperplane is a simplex with vertices corresponding to the vertices of the simplex S_x. This is illustrated in Fig.3. The simplex $S_p = \left\{ y \in R^l : y = x/(x^T \mu), r \in C_p \right\}$ is the projective projection of the convex cone C_p onto the plane $x^T \mu = 1$, where the choice of μ ensures that there are no observed vectors orthogonal to it.

After identifying S_p, the VCA algorithm iteratively projects data onto a direction orthogonal to the subspace spanned by the endmembers already derternined. The new endmember signature corresponds to the extreme of the projection. Fig.3 shows the two iterations of the VCA algorithm applied to the simplex S_p defined by the mixture of two endmembers. In the first iteration, data is projected onto the first direction f_1. The extreme of the projection corresponds to endmember m_a. In the next iteration, endmember m_b is found by projecting data onto direction f_2, which is orthogonal to m_a. The algorithm iterates until the number of endmembers is exhausted.

Nascimento (2005, 2006) compared the VCA with PPI and N-FINDR algorithms by several experiments using simulated data. Conclusions are achieved including that VCA performs better than PPI and better than or similarly to N-FINDR, and secondly, VCA has the lowest computation complexity amone these three algorithms, especially for large dataset.
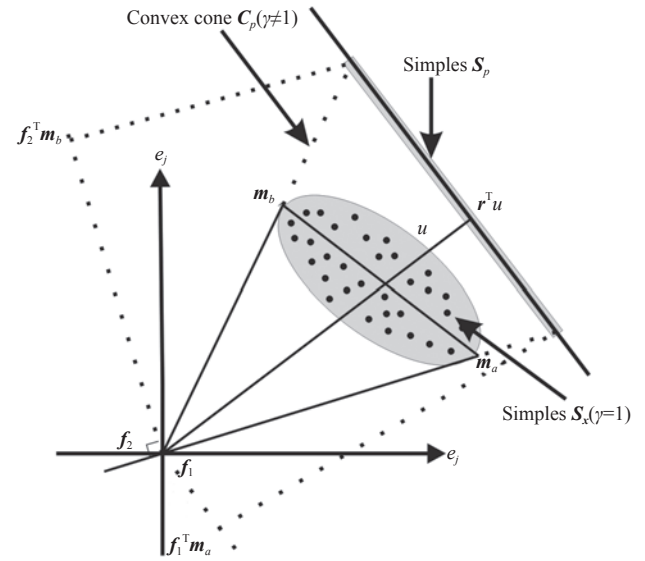

Fig. 3   Illustration of the VCA Algorithm

2.3   SGA

SGA is an improvement of N-FINDR algorithm. It finds a desired p-1 dimensional simplex with the largest volume by gradually growing simplexes vertex by vertex. In other words, it makes an attempt to directly find a p-vertex simplex with the largest volumes by increasing vertices from 2 to p. Its main procedures can be described in detail as follows.

(1)Initialization: use the VD to estimate the number of endmembers.

(2)Randomly generate a target pixel, denoted by t, and find a pixel A_1 that yields the maximum of absolute determinant of the matrix $\left| \det \begin{bmatrix} 1 & 1 \\ t & r \end{bmatrix} \right|$ over all sample vectors r, *i.e.*,

$$A_1 = \arg \left\{ \max_r \left[\left| \det \begin{bmatrix} 1 & 1 \\ t & r \end{bmatrix} \right| \right] \right\} \qquad (5)$$

where PCA or MNF is required to reduce the original data dimensionality to the dimension 2 to find the maximum, set $n=1$, where n is the number of endmembers that have been extracted(the generation of the first endmember pixel A_1 is determined by the randomly generately target pixel t. Chang, *et al.* (2006) shows that the generated A_1 is always a pixel which has either a maximum or a minimum value in the first component of dimensionality reduction transform, and it eventually becomes one of the final generated endmembers).

(3) At $n \geqslant 1$ and for each sample vector, calculate $V(A_1, A_2, \cdots, A_n, r)$ defined by

$$V(A_1, A_2, \cdots, A_n, r) = \frac{\left| \det \begin{bmatrix} 1 & 1 & \cdots & 1 & 1 \\ A_1 & A_2 & \cdots & A_n & r \end{bmatrix} \right|}{n!} \qquad (6)$$

A DR algorithm such as PCA or MNF is required to reduce the original data dimensionality l to be the dimension n.

(4)Find the $(n+1)$th endmember that yields the maximum of $A_{n+1} = \arg \{ \max_r [V(A_1, A_2, \cdots, A_n, r)] \}$.

(5)Stopping rule: if $n < p$, then $n = n+1$ and go step (2). Otherwise,

the final set of $(A_1, A_2, \cdots, A_p)$ is the desired endmember set.

2.4 OSP

In 1994, Harsanyi(1994) firstly used the OSP to detect the desired object. Its virtue is that it can extract interested signatures after aparting gradually the spectras. Initially, OSP needs the prior information of the end-members. After some improvements(Wu, *et al.*, 2004; Chang, 2003;Chang, *et al.*, 2001), it has been used as an endmember extraction algorithm.

The main procedures of OSP to extract the endmembers are as follows:

(1)According to the convex geometry, get the first candidate endmember using the maximum spectral Euclidian distance as Eq. (7). It is the brightest pixel on the image.

$$d = \arg_{x_i}[\max(x_i^{\mathrm{T}} x_i)] \tag{7}$$

(2) Judge the candidate endmember whether it is a noise vector, if is, eliminate the noise pixel.

Wu,*et al.* (2004) designed a noise judgement method that first take the candidate endmember pixel as the window center, and then search for the pixels which have the similar spectral feature with the candidate endmember in the window. If the number of the similar pixels is larger than a threshold, assign the center pixel as an endmember, other wise, it is a noise pixel.

(3)Eliminate the effects of the extracted endmembers for the spectral data, and generate a new spectral data. The main theory of eliminating the effects of the extracted endmembers of OSP algorithm is shown below.

Decompose the matrix A into two parts, $A=[D, U]$, where $D=[d_1, d_2, \ldots, d_w]$ is endmember matrix constructed by the extracted endmembers(desired signatures), w is the number of the extracted endmembers, and U is the endmember matrix constrcted by the remaining endmembers(undesired signatures). At the same time, the abundance vector s is decomposed into two corresponding parts, $s=[s_D, s_U]^{\mathrm{T}}$, then the Eq. (1) can be written as

$$x=Ds_D+Us_U+\varepsilon \tag{8}$$

where P_D is the orthogonal projection matrix of D.

$$P_D=I-D(D^{\mathrm{T}}D)^{-1}D^{\mathrm{T}} \tag{9}$$

where I is the identity matrix, then the matrix P_D can be calculated. The new hyperspectral image can be generated using P_D and the image matrix.

$$P_Dx=P_DUs_U \tag{10}$$

Spectras in the new generated hyperspectral image do not contain the information of the extracted endmember matrix D.

(4)Consider the stopping rules (*e.g.* if the number of the endmembers reaches the given number, *etc.*), if they are met, stop the iteration, output the end-member results. Otherwise, generate the new hyperspectral convex simplex, and iterate the procedures(1)—(3).

3 ENDMEMBER GENERATION ALGORITHM

3.1 ICE

The ICE algorithm has been patented that combines the convex geometry model with suitable assumptions about errors in the model and appropriates statistical procedures to extract more detailed information from hyperspectral image than that of MVT, and

N-FINDR algorithms(Berman, *et al.*, 2003).

The goals of ICE are as follows:

(1)It does not assume that all the endmembers have pure pixel representation in the scene.

(2)It has some resistances to the presence of noises.

(3)It provides a measure for assessing goodness of fit, and in particular for estimating the number of end-members in the scene.

ICE algorithm's main procedures and theory can be found in Berman (2003, 2004).

Spectral unmixing can acuqire the appropriate end-members and abundances according to minimizing the Residual Sum of Squares(RSS) indicated by Eq. (11).

$$\mathrm{RSS} = \sum_{i=1}^{N}(x_i - \sum_{k=1}^{p} S_{ik} A_k)^{\mathrm{T}}(x_i - \sum_{k=1}^{p} S_{ik} A_k) \tag{11}$$

ICE uses an alternative representation of RSS as Eq.(12)

$$\mathrm{RSS} = \sum_{j=1}^{d}(x_j - SA_j)^{\mathrm{T}}(x_j - SA_j) \tag{12}$$

where x_j denotes the N observations in the jth MNF band. A_j is the p-vector of endmember values in the jth MNF band, and S is the $N\times p$ matrix of proportions of the p endmembers for all the image pixels. It can be shown that the minimizer of Eq.(11) or Eq.(12) is any p-simplex in the hyperplane spanned by the first $p-1$ MNF bands, which totally encloses the data points projected onto the hyperplane.

In order to constrain the size of the simplex somehow while keep faithful to the model. One way of doing this is by adding a term to Eq.(11) or Eq.(12) which is proportional to a measure of the size of the simplex. ICE uses the Sum of Squared Distance(SSD) between all the simplex vertices, which is computationally cheaper.

$$\mathrm{SSD} = \sum_{k=1}^{p-1}\sum_{l=k+1}^{p}(A_k - A_l)^{\mathrm{T}}(A_k - A_l) \tag{13}$$

Berman(2003) shows that SSD can be written as

$$\mathrm{SSD}=p(p-1)V \tag{14}$$

where V is the sum fo the variances of the simplex vertices.

The objective function of ICE is

$$\mathrm{RSS}_{\mathrm{reg}}=(1-\mu)\mathrm{RSS}/N+\mu V \tag{15}$$

where μ is a small "tradeoff" of "regularization" parameter in (0, 1). Eq. (15) needs to be minimized over both the p endmembers and the p proportions for each pixel. One solution is to minimize (15) iteratively: given the endmember estimates, estimate the proportion matrix S, this just involve the separate LS minimization of each of the N terms in Eq.(12), subject to the abundance constraints. Then, with given S, calculate each A_j using the following equation

$$A_j = \left\{ S^{\mathrm{T}}S + \lambda(I_M - 11^{\mathrm{T}}/p) \right\}^{-1} S^{\mathrm{T}}x_j \tag{16}$$

where $\lambda=N\mu/[(p-1)(1-\mu)]$. The algorithm stops iterating when the ratio of successive values of $\mathrm{RSS}_{\mathrm{reg}}$ is less than a tolerance.

Berman(2003, 2004) indicates that we can obtain a more exact endmember number using the implementation of ICE algorithm time after time, and acquire preferable experimental results for the AVIRIS data of Oatman areas.

3.2 MVC-NMF

The MVC-NMF algorithm integrates the least squares analysis and the convex geometry model by incorporating a volume constraint into the NMF formulation. The proposed cost function consists of two parts. One part measures the approximation error between the observed data and the reconstructions from the esti-

mated endmembers and abundances, and the other part consists of the minimum volume constraint. Miao(2007) treats these two terms serving as two forces: the external force (minimizing the approximation error) drives the estimation to move outward of the data cloud, and the internal force (minimizing the simplex volume) acts in the opposite direction by forcing the endmembers to be as close to each other as possible. Its main procedures are described as:

(1)Estimate the number of the endmembers using the VD method.

(2)Construct the following cost function

$$
\begin{cases}
\min f(\boldsymbol{A}, \boldsymbol{S}) = \dfrac{1}{2} \| \boldsymbol{X} - \boldsymbol{A}\boldsymbol{S} \|_F^2 + \lambda J(\boldsymbol{A}) \\
\boldsymbol{A}_{i,j} \geqslant 0, \boldsymbol{S}_{i,j} \geqslant 0, 1_p^{\mathrm{T}}\boldsymbol{S} = 1_n^{\mathrm{T}}
\end{cases} \tag{17}
$$

where $1_p(1_n)$ is a p(n)-dimensional column vector of all 1s, $J(A)$ is the penalty function, calculating the volume determined by the estimated endmembers. The regularization parameter $\lambda \in \mathbf{R}$ is used to control the tradeoff between the accurate reconstruction and the volume constraint.

(3)Initialization: Choose randomly p points from the given data and arrange them as the columns of the initial matrix $\boldsymbol{A}$. The value of $\boldsymbol{S}$ can also be randomly initialized, or initialized to be the zero matrix.

(4)Stopping conditions: the most commonly used methods are the maximum iteration number and the error tolerance.

(5)Minimize the objective function with respect to both $\boldsymbol{A}$ and $\boldsymbol{S}$ according to some rules. If the stopping conditions are satisfied, stop the iteration procedure, or update the matrix $\boldsymbol{A}$ and $\boldsymbol{S}$, searching for the matrixes that can be minimizing the objective function.

4 EXPERIMENTS AND ANALYSIS

4.1 Experimental Objectives

The experiments and analysis were taken to evaluate the six EEAs using the synthetic and real hyperspectral image data. The experiments included: (1)comparison of unmixing results with different endmember number; (2)comparison of robustness for noise; (3)comparison of endmember extraction results with different image size; (4)experiments with real hyperspectral data.

4.2 The Endmember Similarity Metric

To evaluate the experimental results, the Spectral Angle Distance(SAD), SID(Spectral Information Divergence), AAD(Abundance Angle Distance), AID(Abundance Information Divergence) proposed by Nascimento(2005) are adopted. Eq. (18) (19) denote the similarity measure, where $\boldsymbol{a}$ and $\hat{\boldsymbol{a}}$ are true spectra and estimated spectra, respectively. $\boldsymbol{P} = \boldsymbol{a} / \sum_{i=1}^{l} \boldsymbol{a}_i$ is the probability distributing vector.

$$
\mathrm{SAD} = \cos^{-1}\left(\frac{\boldsymbol{a}^{\mathrm{T}}\hat{\boldsymbol{a}}}{\|\boldsymbol{a}\| \cdot \|\hat{\boldsymbol{a}}\|} \right) \tag{18}
$$

$$
\begin{cases}
\mathrm{SID} = \boldsymbol{D}(\boldsymbol{a} \mid \hat{\boldsymbol{a}}) + \boldsymbol{D}(\hat{\boldsymbol{a}} \mid \boldsymbol{a}) \\
\boldsymbol{D}(\boldsymbol{a} \mid \hat{\boldsymbol{a}}) = \sum_{i=1}^{l} p_i \log\left(\dfrac{p_i}{\hat{p}_i} \right) \\
\boldsymbol{P} = \boldsymbol{a} / \sum_{i=1}^{l} \boldsymbol{a}_i
\end{cases} \tag{19}
$$

*Berman(2009) indicated that only using the key pixels can improve the ICE algorithm's efficiency, this method can also be used for the other five EEAs, so the experiments are all not using this method

4.3 Experimental Data Description

The synthetic data was created with the USGS spectral library(Clark, 2007), and the spectras in this library contained 224 spectral bands covering wavelengths from 0.38—2.5 μm with a spectral resolution of 10 nm(we used 188 bands in the experiments). The synthetic hyperspectral data with sizes of 64×64, 81×81 and 100×100 were created. The abundance of the pixel in the data was created randomly, and meantime, the abundances of each pixel fulfill the ANC and ASC. We replaced the pixels whose maximum abundance was larger than 0.8 with a mixture made up of all endmembers of equal abundances. To simulate possible errors and sensor noise, we added zero-mean Gaussian noise to the mixture data.

The real hyperspectral data collected by the AVIRIS sensor over Cuprite, Nevada, was acquired on the AVIRIS flight of July, 1997. The size of the subimage was 100×100. AVIRIS instrument covers the spectral region from 0.4—2.5 μm in 224 bands with a 10 nm bandwidth and a 20 m spatial resolution. To improve the unmixing performance, we removed the low SNR bands as well as the water-vapor absorption bands(including bands 1—2, 104—113, 148—167, 221—224) from the original 224-band data cube. Therefore, a total of 188 bands were used in the experiment. The image data was converted into the reflectance data using the ATREM (Atmospheric Removal) (Gao, *et al*., 1990) method. The remnant error was minimized using the EFFORT (Empirical Flat Field Optimized Reflectance Transform) (Boardman, 1998) method. The false color image of the subimage is illustrated as Fig.4(R: 7the band, G: 32th band, B: 62th band).
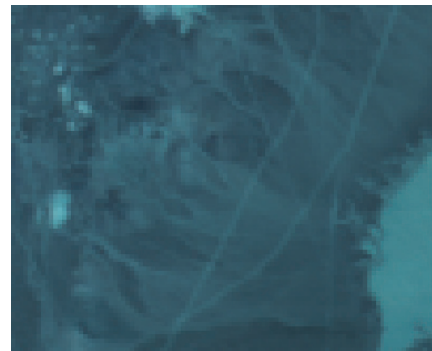

Fig.4　The experimental subimage of Cuprite area

4.4 Experimental Result and Analysis

The maximum iteration number of ICE* and MVC-NMF algorithms was set to be 150, λ=0.05. They were all initialized using the VCA and Fully Constrained Least Squares(FCLS)(Hei, *et al*., 2001) methods. The unit of SAD in the following tables was degree. The experiments were based on the Matlab 7.0 platform, using 2.68 GHz CPU, and 1G EMS memory.

4.4.1 Comparison of unmixing results with different endmember number

The objective of this part is to compare the six EEAs with different endmembers number.. In the experiments, the synthetic image size is 64×64, the SNR of the noise in the mixed data is 30 db.

The experimental results with the endmembers' number is 4, 5, 6, and 7, respectively, are listed in Table 1 and Table 2. The 2-D projection of the simulated data, true endmembers and the end-members with the six EEAs are plotted in Fig.5. From the results, we can see that the EEA order from the high precision to low precision is: MVC-NMF, ICE, VCA, OSP, N-FINDR and SGA, and from high efficiency to low efficiency is: OSP, VCA, SGA, N-FINDR, MVC-NMF and ICE.

4.4.2 Robustness comparison for the noise

To illustrate the robustness effect to noise corruptions, the synthetic data is created using four spectras, the Gaussian noise with SNR = 20 db, 30 db, 40 db and 50 db are added into the mixed data. The endmember extraction results and the consuming time using the six EEAs are listed in Table 3 and Table 4. Fig.6 and Fig.7 illustrates the plot of the true endmembers and extracted endmembers when the noise SNR is 20 db and 40 db, respectively. From these results, we can see that the algorithms become inappropriate with decreasing SNR values. The robustness order to the noise from high to low is: MVC-NMF, ICE, VCA, OSP, N-FINDR and SGA. From high efficiency to low efficiency, the EEA order is: OSP, VCA, SGA, N-FINDR, MVC-NMF and ICE when the noise SNR is different.

4.4.3 Comparison of endmember extraction results with different image size

The objective of this part is to compare the six EEAs with the different image sizes. The synthetic data is created using four spectras, and the SNR of the noise in the mixed data is 30 db. The experiments results when the image size is 64×64, 81×81, and 100×100 are listed in Table 5 and Table 6. From the results, we can see that the EEA order from the high precision to low precision is: MVC-NMF, ICE, VCA, OSP, N-FINDR and SGA. From the consuming time listed in Table 6, the efficiency order of the EEAs from high to low is: OSP, VCA, SGA, N-FINDR, MVC-NMF and ICE.

4.4.4 Experiments with real hyperspectral image data

The estimated number of endmembers for the Cuprite area AVIRIS image data using VD method is 9. The endmember extraction results can be compared with the spectras in the USGS library(Winter, 1999a; Nascimento, 2006; Berman, et al., 2003; Miao, et al., 2007). The experimental results are listed in Table 7. From the results, we can see that for the real hyperspectral image data, the EEA order from the high precision to low precision is: MVC-NMF, ICE, N-FINDR, VCA, SGA and OSP. From the consuming time listed in Table 8, we can see that the efficiency order of the EEAs from high to low is: OSP, VCA, SGA, N-FINDR, MVC-NMF and ICE.

The results are somewhat different between the synthetic image data and the real hyperspectral data. Specifically, the precision of the VCA is a little lower than the N-FINDR. This is not contradicted with the results of Nascimento(2006): VCA performs better than or similarly to N-FINDR, but its efficiency adbantage is obvious.

From the experimental results, we can conclude that EIA has a high efficiency, but a low precision. The reason is that the EIA searches for the representative pixels in the image data as the extracted endmembers, but the EGA generates the endmembers with some optimization principle. The experimental results are in accordance with the theory analysis.

Table 1   Experimental results with different endmember number

Endmember number	N-FINDR		VCA		SGA		OSP		ICE		MVC-NMF	
	SAD	SID	SAD	SID	SAD	SID	SAD	SID	SAD	SID	SAD	SID
4	3.908	0.013	3.293	0.011	7.483	0.053	3.908	0.013	5.273	0.033	2.409	0.005
5	12.142	0.066	11.434	0.062	16.111	0.161	13.778	0.079	9.747	0.031	5.450	0.032
6	9.674	0.066	9.235	0.039	13.466	0.111	7.945	0.033	5.308	0.023	1.614	0.002
7	11.034	0.097	11.769	0.089	9.009	0.066	10.881	0.096	6.452	0.033	3.022	0.008

Table 2   The consuming time of the EEAs with different endmember number

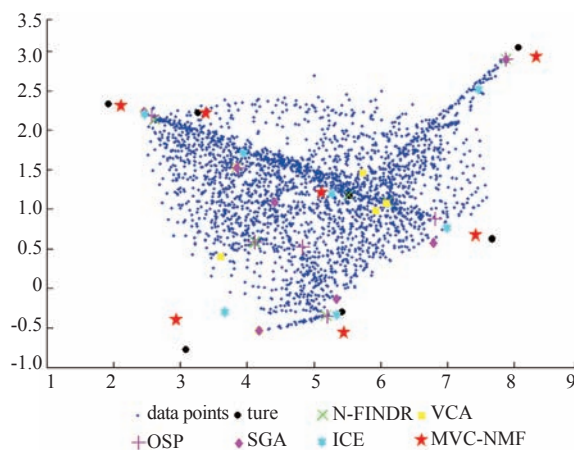| Endmember number	Consuming time/s					
	N-FINDR	VCA	SGA	OSP	ICE	MVC-NMF
4	4.9	0.5	0.9	0.4	542.2	110.4
5	4.8	0.5	0.9	0.5	689.9	120.7
6	5.0	0.5	1.1	0.4	824	174.4
7	5.3	0.5	1.1	0.6	941	273.5

Fig.5   2D projection of the endmember extraction results with the endmember number of 7

Table 3   Robustness comparison with different noise SNR

SNR/db	N-FINDR		VCA		SGA		OSP		ICE		MVC-NMF	
	SAD	SID	SAD	SID	SAD	SID	SAD	SID	SAD	SID	SAD	SID
20	7.379	0.037	3.265	0.012	10.996	0.081	7.349	0.035	3.054	0.013	1.019	0.0009
30	3.908	0.013	3.293	0.011	7.483	0.053	3.908	0.013	3.073	0.010	2.409	0.005
40	2.621	0.005	2.808	0.005	4.411	0.011	2.589	0.005	2.071	0.004	0.575	0.0004
50	2.910	0.006	3.651	0.012	2.907	0.006	2.697	0.006	2.403	0.010	0.422	0.0001

Table 4   The consuming time of the EEAs with different noise SNR

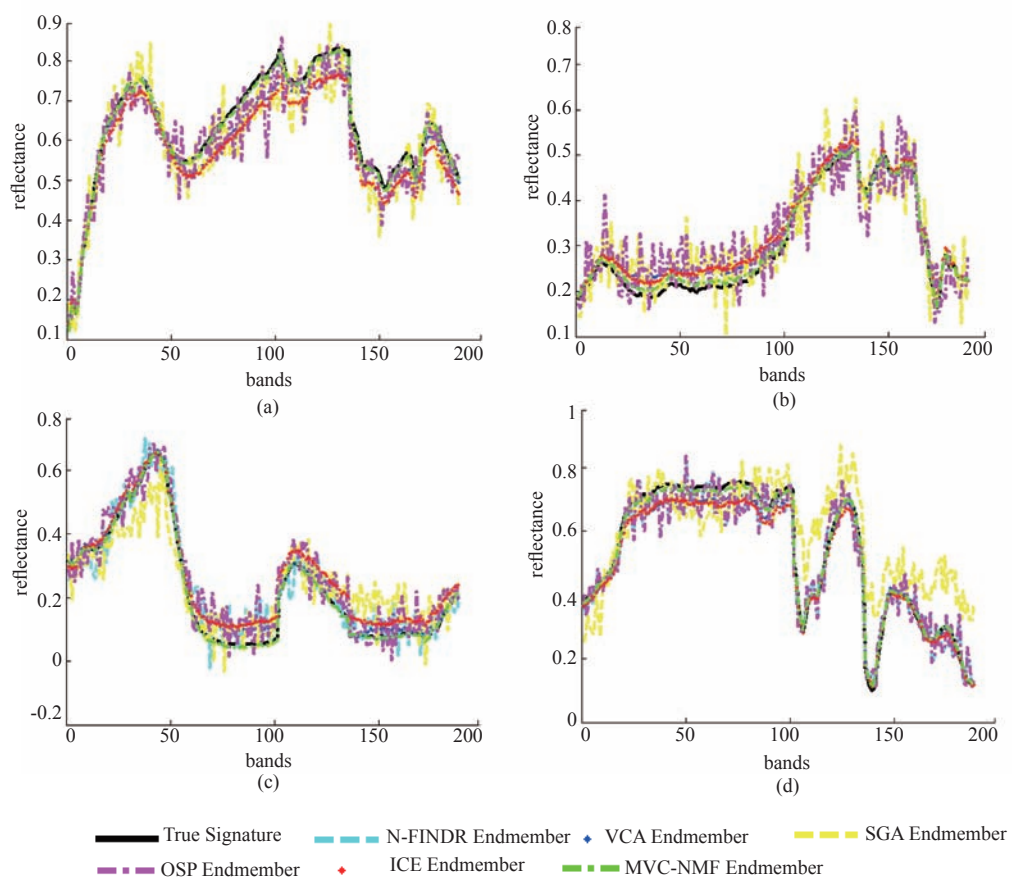| SNR/db	Consuming time/s					
	N-FINDR	VCA	SGA	OSP	ICE	MVC-NMF
20	5.1	0.5	0.8	0.4	563.4	120.1
30	4.9	0.5	0.9	0.4	542.2	110.4
40	4.8	0.9	0.8	0.4	541.6	117.5
50	6.3	0.6	0.8	0.4	588.5	126.1

Fig.6   Endmember extraction results with the SNR of 20 db
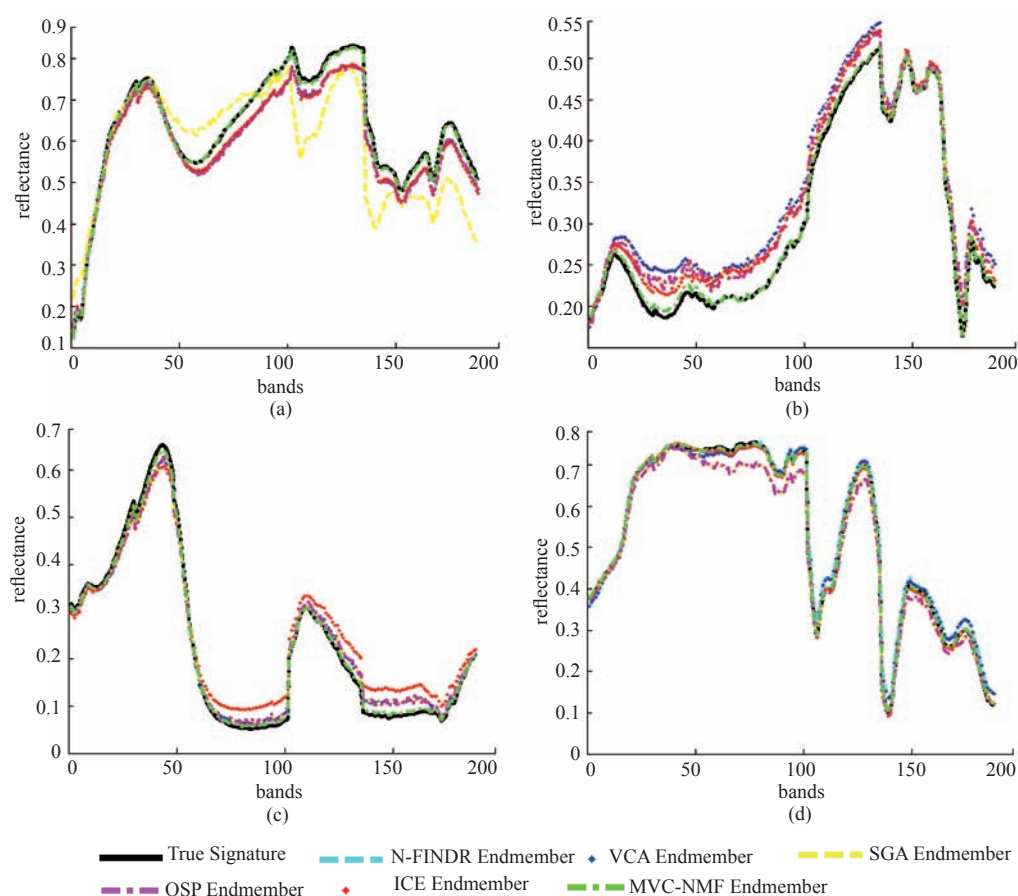(a) Endmember–1; (b) Endmember–2; (c) Endmember–3; (d) Endmember–4

Fig.7   Endmember extraction results with the SNR of 40 db
(a) Endmember–1; (b) Endmember-2; (c) Endmember–3; (d) Endmember-4

Table 5   Result comparison with different image size

Image size/pixel	N-FINDR		VCA		SGA		OSP		ICE		MVC-NMF	
	SAD	SID	SAD	SID	SAD	SID	SAD	SID	SAD	SID	SAD	SID
64×64	3.908	0.013	3.293	0.011	7.483	0.053	3.908	0.013	3.273	0.012	2.409	0.005
81×81	2.511	0.005	1.286	0.001	2.632	0.006	2.526	0.005	1.147	0.001	0.347	0.0001
100×100	2.136	0.003	0.992	0.001	2.194	0.003	2.101	0.003	0.874	0.001	0.279	0.0001

Table 6   The consuming time of EEAs with different image size

Image size/pixel	Consuming time/s					
	N-FINDR	VCA	SGA	OSP	ICE	MVC-NMF
64×64	4.9	0.5	0.9	0.4	542.2	110.4
81×81	8.3	0.7	1.1	0.5	719	137.7
100×100	12.4	0.8	1.4	0.9	902	347

Table 7   Endmember extraction results for the real hyperspectral image data

Image size/pixel	N-FINDR		VCA		SGA		OSP		ICE		MVC-NMF	
	SAD	SID	SAD	SID	SAD	SID	SAD	SID	SAD	SID	SAD	SID
100×100	6.192	0.021	6.491	0.023	6.991	0.028	8.080	0.031	5.623	0.019	5.025	0.012

Table 8   The consuming time of the EEAs for the real hyperspectral image data

Image size/pixel	Consuming time/s					
	N-FINDR	VCA	SGA	OSP	ICE	MVC-NMF
100×100	13.1	0.9	1.5	0.9	909	354

5   CONCLUSION

Solving the problem of the mixel can not only realize the high-precision classification and the sub-pixel object recognition, but also ensure more adequately use the hyperspectral image. According to the analysis of some classical EEAs, these algorithms can be classified into two categories: Endmember Identification Algorithm and Endmember Generation Algorithm. The six endmember extraction algorithms in common use are summarized and experimented, the following conclusions can be drawn:

(1)From the perspective of precision for the EEAs, EGAs are better than the EIAs. With the six algorithms, MVC-NMF extracts the most accurate endmember results. Although the SGA is an improvement of N-FINDR, it does not outperform the N-FINDR algorithm.

(2)From the perspective of efficiency for the EEAs, EIAs are better than the EGAs, especially for the VCA and OSP. Compared with N-FINDR, SGA has a higher efficiency.

Each EEA has its shortcomings, and in order to obtain better mixel decomposition results, it is insufficient to take into account one class EEA. According to the advantages and disadvantages for the two kinds of EEAs, some prospects are put forward for the study of EEA in the next stage:

(1)If the efficiency is weighted in practice, we can use EIA to extract the endmembers, especially for the VCA and OSP, both of which have higher efficiency and relative higher precisions. If high precision of the endmember extraction to be acquired, EGA can be adopted to implement the endmember extraction, and MVC-NMF is better than ICE algorithm.

(2)The EGA can be initialized using the EIA results, which can improve the efficiency of EGA. For example, VCA has a high efficiency and its precision is relative higher than the other EIAs. Thus it can be used to initialize the EGAs, such as ICE and MVC-NMF, which can speed up the convergence of the algorithms and the reliability of the endmember extraction results.

(3)Before the mixel decomposion, the initial end-members can be extracted using the EIAs, then the pixels within the initial simplex whose vertices are the initial endmembers can be eliminated(the abundance of these pixels fulfill the ANC and ASC). Using the EGA for the pixels out of the initial convex hull can improve the efficiency of the algorithms and the reliability of the end-member extraction results.

REFERENCES

Berman M, Kiiveri H, Lagerstrom R, Ernst A, Dunne R and Hunt-ington J F. 2003. ICE: an automated statistical approach to iden-tifying endmembers in hyperspectral images. IEEE International Geoscience and Remote Sensing Symposium, France: Toulouse, **1**: 279–283

Berman M, Kiiveri H, Lagerstrom R, Ernst A, Dunne R and Huntington J F. 2004. ICE: a statistical approach to identifying endmembers in hyperspectral images. *IEEE Transactions on Geoscience and Remote Sensing*, **42**(10): 2085–2095

Berman M, Phatak A, Lagerstrom R and Wood B R. 2009. ICE: a new method for the multivariate curve resolution of hyperspectral im-ages. *Journal of Chemometrics*, **23**(2): 101–116

Boardman J W. 1998. Post-ATREM polishing of AVIRIS apparent reflectance data using EFFORT: a lesson in accuracy versus preci-sion. Summaries of the Seventh JPL Airborne Earth Science Work-shop. Pasadena: JPL Publication

Boardman J W, Kruse F A and Green R O. 1995. Mapping target sig-natures via partial unmixing of AVIRIS data: in Summaries. Fifth JPL Airborne Earth Science Workshop. Pasadena: JPL Publication: 23–26

Bowles J H, Palmadesso P J, Antoniades J A, Baumbeck M M and Rickard L J. 1995. Use of filter vectors in hyperspectral data anal-ysis. Infrared Spaceborne Remote Sensing III, SPIE Proceedings. San Diego, USA, **2553**: 148–157

Chang C I. 2003. Hyperspectral Imaging: Techniques for Spectral De-tection and Classification. New York: Kluwer Academic/Plenum Publishers: 40–41

Chang C I, Du Q, Chiang S S, Heinz D C and Ginsberg I W. 2001. Unsupervised target subpixel detection in hyperspectral imagery. Conference Algorithms for Multispectral, Hyperspectral, and Ultraspectral Imagery VII, SPIE Proceedings. Orlando FL, USA, **4381**: 370–379

Chang C I, Wu C C, Liu W M and Ouyang Y C. 2006. A new grow-ing method for simplex-based endmember extraction algorithm. *IEEE Transactions on Geoscience and Remote Sensing*, **44**(10): 2804–2819

Clark R N, Swayze G A, Wise R, Livo K E, Hoefen T M, Kokaly R F and Sutley S J. 2007. splib06b. USGS Digital Spectral Library. [2009-11-3]. http://speclab.cr.usgs.gov/spectral-lib.html

Craig M D. 1994. Minimum-volume transforms for remotely sensed data. *IEEE Transactions on Geoscience and Remote Sensing*, **32**(3): 542–552

Gao B C and Goetz A F H. 1990. Column atmospheric water vapor and vegetation liquid water retrievals from airborne imaging spectrom-eter data. *Journal of Geophysical Research*, **95**(D4): 3549–3564

Gruninger J H, Ratkowski A J and Hoke M L. 2004. The sequential maximum angle convex cone (SMACC) endmember model. Algo-rithms for Multispectral, Hyperspectral and Ultraspectral Imagery X, SPIE Proceedings. Orlando, USA, **5425**: 1–14

Harsanyi J C and Chang C I. 1994. Hyperspectral image classification and dimensionality reduction: an orthogonal subspace projection

approach. *IEEE Transactions on Geoscience and Remote Sensing*, **32**(4): 779–785

Heinz D C and Chang C I. 2001. Fully constrained least squares linear spectral mixture analysis method for material quantification in hyperspectral imagery. *IEEE Transactions on Geo-science and Remote Sensing*, **39**(3): 529–545

Ifarraguerri A and Chang C I. 1999. Multispectral and hyperspectral image anlysis with convex cones. *IEEE Transactions on Geoscience and Remote Sensing*, **37**(2): 756–770

Kumar A and Min H A. 2008. Some issues related with sub-pixel classification using Hyperion data. ISPRS XXI VII, Beijing: ISPRS

Miao L D and Qi H R. 2007. Endmember extraction from highly mixed data using minimum volume constrained nonnegative matrix factorization. *IEEE Transactions on Geoscience and Remote Sensing*, **45**(3): 765–777

Nascimento J M P. 2006. Supervised Hyperspectral Unmixing. Lisboa: Universidade Técnico de Lisboa: 47–72

Nascimento J M P and Dias J M B. 2005. Vertex component analysis: a fast algorithm to unmix hyperspectral data. *IEEE Transactions on Geoscience and Remote Sensing*, **43**(4):898–910

Neville R A, Staenz K, Szeredi T, Lefebvre J and Hauff P. 1999. Automatic endmember extraction from hyperspectral data for mineral exploration. Proceedings of Fourth International Airborne Remote Sensing Conference and Exhibition/21st Canadian Symposium on Remote Sensing. Ottawa, Canada: 21–24

Plaza A and Chang C I. 2005. An improved N-FINDR algorithm in implementation. Algorithms and Technologies for Multispectral, Hyperspectral and Untraspectral Imagery XI, SPIE Proceedings.

Orlando, USA, **5806**: 298–306

Plaza A and Chang C I. 2006. Impact of initialization on design of endmember extraction algorithms. *IEEE Transactions on Geoscience and Remote Sensing*, **44**(11): 3397–3407

Winter M E. 1999a. N-FINDR: an algorithm for fast autonomous spectral endmember determination in hyperspectral data. Imaging Spectrometry V, SPIE Proceedings. Denver CO, USA, 3753: 266–275

Winter M E. 1999b. Fast autonomous spectral end-member determination In hyperspectral data. Proceedings of the Thirteenth International Conference on Applied Geologic Remote Sensing. Vancouver, B C, Canada: 337–344

Winter M E. 2004. A proof of the N-FINDR algorithm for the automated detection of end-members in a hysperspectral image // Algorithms and Technologies for Multispectral, Hyperspectral, and Ultraspectral Imagery X, SPIE Proceedings. Orlando, USA: 12–15

Wu B, Zhang L P and Li P X. 2004. Unsupervised orthogonal sub-space projection approach to unmix hyperspectral imagery automatically. *Journal of Image and Graphics*, **9**(11): 1392– 1396

Zhang J K, Rivard B and Rogge D M. 2008. The successive projection algorithm (SPA), an algorithm with a spatial constraint for the automatic search of endmembers in hyperspectral data. *Sensors*, **8**: 1321–1342

Zhang X, Tong X H and Liu M L. 2009. An improved N-FINDR algorithm for endmember extraction in hyperspectral imagery. Urban Remote Sensing Joint Event. Shanghai, China

高光谱图像端元提取算法研究进展与比较

李二森[1, 2]，朱述龙[1]，周晓明[1]，余文杰[1]

1. 信息工程大学 测绘学院，河南 郑州 450052；
2. 矿山空间信息技术国家测绘局重点实验室，河南 焦作 454000

摘　要：高光谱图像中混合像元的存在不仅影响了基于遥感影像的地物识别和分类精度，而且已经成为遥感科学向定量化方向发展的主要障碍。本文分析和研究了现有的典型端元提取算法，在此基础上，对这些算法进行归纳总结，从是否假定纯像元存在角度将其分为两类：端元识别算法和端元生成算法，并就两种分类方法选取了具有代表性的6种典型端元提取算法：N-FINDR、VCA、SGA、OSP、ICE和MVC-NMF算法进行分析和实验。通过对这6种方法的实验比较，得出两种端元提取分类方法的优点与不足，并对今后的研究工作提出展望。

关键词：高光谱图像，混合像元，线性光谱混合模型，端元

中图分类号：TP79　　　文献标志码：A

1 引　言

混合像元在高光谱图像中广泛存在，混合像元分解是解决混合像元问题实现子像元分类的有效途径(Kumar和Min，2008)。目前为止，线性光谱混合模型(LSMM，Linear Spectral Mixture Model)仍是国内外研究最深入、应用最广泛的混合像元分解模型，主要步骤包括：数据降维DR(Dimension Reduction)、端元提取EE(Endmember Extraction)和丰度估计AE(Abundance Estimation)3部分，其中端元提取是混合像元分解的关键。根据是否假定光谱数据中存在纯像元，端元提取算法可以分为两类(Plaza和Chang，2005)：端元识别算法EIA(Endmember Identification Algorithm)和端元生成算法EGA(Endmember Generation Algorithm)，EIA直接从光谱数据中提取端元(即假定影像中存在纯像元)，算法的理论一般比较简单，而EGA是从光谱数据中产生端元，算法的过程较为复杂。对于高光谱数据而言，由于地面分辨率等因素的限制，在大多数情况下，数据中并不存在纯像元，因此，EGA算法在理论上提取的端元精度较高。

基于线性光谱混合模型的端元识别算法主要有像元纯度指数PPI(Pixel Purity Index)(Boardman 等，1995)、N-FINDR(Winter，1999a，1999b，2004)、序列最大角度凸锥SMACC(Sequential Maximum Angle Convex Cone)(Gruninger 等，2004)、顶点成分分析VCA(Vertex Component Analysis) (Nascimento 和 Dias，2005；Nascimento，2006)、单体增长算法SGA(Simplex Growing Algorithm)(Chang 等，2006)、正交子空间投影算法OSP(Orthogonal Subspace Projection)(Harsanyi 和 Chang，1994)、序列投影算法SPA(Sequential Projection Algorithm)(Zhang 等，2008)等。端元生成算法主要有极小体积变换MVT(Minimum Volume Transform)(Craig 等，1994)、凸锥分析算法CCA(Convex Cone Analysis)(Ifarraguerri 和Chang，1999)、迭代误差分析IEA(Iterative Error Analysi)(Neville 等，1999)、ORASIS(Bowles 等，1995)、迭代限制端元ICE(Iterated Constrained End-

member)(Berman 等，2003，2004)、最小体积限制的非负矩阵分解MVC-NMF(Minimum Volume Constraint Nonnegative Matrix Factorization)(Miao 和 Qi，2007)。本文重点对 N-FINDR、VCA、SGA 和 OSP 4种端元识别算法和两种端元生成算法(ICE、MVC-NMF)进行了原理分析及实验，并在端元提取结果及效率上进行了比较，分析了各自的优点与不足，为后续研究打下了坚实基础，研究成果及结论也可以为其他研究者提供参考。

2 端元识别算法

文中假定线性光谱混合模型表达式为：

$$x = \sum_{i=1}^{p} A_i s_i + \varepsilon = As + \varepsilon \tag{1}$$

式中，x为l (l为影像波段数)维混合像元光谱，是已知观测量，A为$l \times p(p$为端元数目)端元矩阵或源矩阵(Endmember or Source Matrix)，其中每一列为一个端元的光谱向量，向量s为该像元中各端元的丰度，ε为l维高斯随机噪声或模型误差，图1为线性光谱混合模型的示意图。对于线性光谱混合模型而言，丰度向量s满足两个限制条件：即非负性限制ANC(Abundance Non-negativity Constraint，$s_i \geqslant 0$，i=1，2，…，p)、和为1限制ASC(Abundance Sum-to-one Constraint，$\sum_{i=1}^{p} s_i = 1$)。

$x=As+\varepsilon$
$A=[A_1, A_2, \cdots, A_p]$
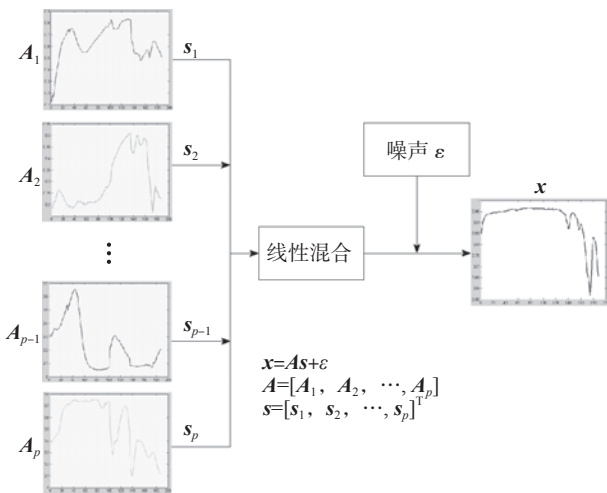$s=[s_1, s_2, \cdots, s_p]^T$

图1 线性光谱混合模型示意图

2.1 N–FINDR算法

N-FINDR算法是基于凸集几何的方法寻找影像

中的纯像元集，该方法认为：在N维光谱空间，由纯像元组成的单体体积比由其他任何像元组合成的体积都大(图2)。该算法由一组随机的像元集开始，在数据内部不断进行单体的"膨胀"，对于每个像元和每个端元，端元被像元的光谱取代，并且体积被重新计算，如果体积增加，新像元的光谱取代该端元，重复执行该过程直到没有任何替代发生为止，Winter(1999a，1999b)利用该算法在合成数据集中成功提取了端元，并且通过实验表明该算法在非完美数据中具有鲁棒性。实验提取了AVIRIS Cuprite数据集的端元，结果与参考数据相吻合，并且丰度图与出版的矿物图一致。Winter(2004) 从理论上进一步对N-FINDR算法进行了解释，从理论上证明了该算法端元提取结果的正确性，并且通过实验证明该算法在处理非理想数据时仍然具有较好的收敛性。

N-FINDR算法具体步骤为：

(1) 指定端元数目p，使用极小噪声分离MNF(Minimum Noise Fraction)对数据进行降维，使其维数降至p–1；

(2)在影像数据块中，随机选择p个像元作为候选端元，并计算端元形成的单体体积V_1，体积计算公式为：

$$V(E) = \frac{1}{(p-1)!} \text{abs}(|E|) \tag{2}$$

$$E = \begin{bmatrix} 1 & 1 & \cdots & 1 \\ A_1 & A_2 & \cdots & A_P \end{bmatrix} \tag{3}$$

式中，A_i为第i个端元所对应的p-1维列向量。

(3)在影像其他像元中选择一个像元P$_1$，取代一个候选端元，形成新的凸面单体，计算体积V_2，如果$V_2>V_1$，则该像点取代候选端元形成新的候选点；
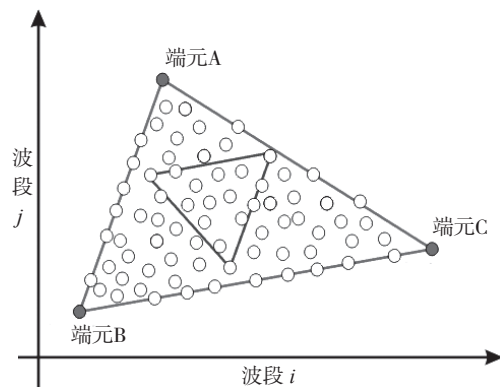
(4)将像点P取代其他候选端元，做同步骤(3)的操作；

图2 二维特征空间中的单体及端元位置

(5)所有其他像元循环执行步骤(3)和(4)，最终形成体积最大的单体，其顶点对应于所有的端元。

Winter(1999a，1999b)指出，N-FINDR算法在一定情况下会遇到困难，真实影像中很可能不包含纯的或接近纯光谱的像元，这时该算法的基本假设(图像中存在纯的像元)不能得到满足，此时算法会找到混合最少的像元作为该端元的最佳估计；另外，如果图像中存在比非混合像元具有更高亮度的混合像元，该算法会选择它们作为端元。

N-FINDR算法有以下几个缺点：(1)没有提供确定端元数目的准则和算法；(2)N-FINDR算法将随机向量作为初始端元，该方法具体实施过程中耗用时间较长；(3)由于初始端元为随机变量，N-FINDR算法产生的最终结果没有重复性；(4)算法需要提前进行降维处理，可能会对端元提取结果造成偏差，并且选择不同的降维方法可能会产生不同的端元提取结果。针对这些缺点，Plaza和Chang(2005)利用虚拟维(VD)确定端元数目，用迭代误差分析算法的端元提取结果作为N-FINDR的初始端元，加快了算法的收敛速度并且端元提取结果更加稳定；Plaza和Chang(2006)研究了端元初始化方法(ATGP(Automatic Target Generation Process)、UFCLS(Unsupervised Fully Constrained Least Squares)、IEA(Iterative Error Analysis)、Maximin-Distance Algorithm)对N-FINDR算法的影响，实验证明引入端元初始化方法不仅可以加快算法的收敛速度并且不少初始端元引入N-FINDR后将会成为最终的端元，尤其是利用ATGP作为初始化方法比其他3种方法获取的结果都更优；Zhang(2009)使用ATGP算法对N-FINDR进行端元初始化，并且利用距离代替体积计算，加快了算法的收敛。

2.2 VCA算法

VCA算法基于凸面几何理论在假设数据中存在纯像元的情况下提取端元，它考虑了由于地表起伏的变化，利用凸锥来对数据进行建模，其在适当选择的超平面上的投影为由端元作为顶点的单体。在将数据投影到选择的超平面上之后，VCA将所有影像上的像元投影到随机方向上，并将具有最大投影的像元作为第一个端元，通过迭代地将数据投影到与由已提取端元构成的子空间正交的方向上的方法来提取其余端元，被极限投影所对应的像元作为新的端元。具体过程为：

假定线性混合模型表达式为：

$$x = A\gamma s + \varepsilon \qquad (4)$$

式中，γ为比例因子，表示由于地表起伏引起的光照变化。由于丰度的物理限制(非负限制、和为一限制)，$s \in \Delta_p$，Δ_p为单体，每个波段可以作为l维空间的坐标轴，每个像元为l维欧氏空间的一个向量，$S_x = \{x \in R^l : x = As, s \in \Delta_p\}$也为单体，$C_p = \{x \in R^l : x = A\gamma s, s \in \Delta_p, \gamma \geqslant 0\}$由于比例参数$\gamma$而是一个凸锥。

凸锥C_p在适当选择的超平面上的投影为以与单体S_x端点相对应的单体，如图3所示。$S_p = \{y \in R^l : y = x/(x^T \mu), r \in C_p\}$为凸锥$C_p$在平面$x^T \mu = 1$上的投影，$\mu$的选择确保没有观测向量与其正交。
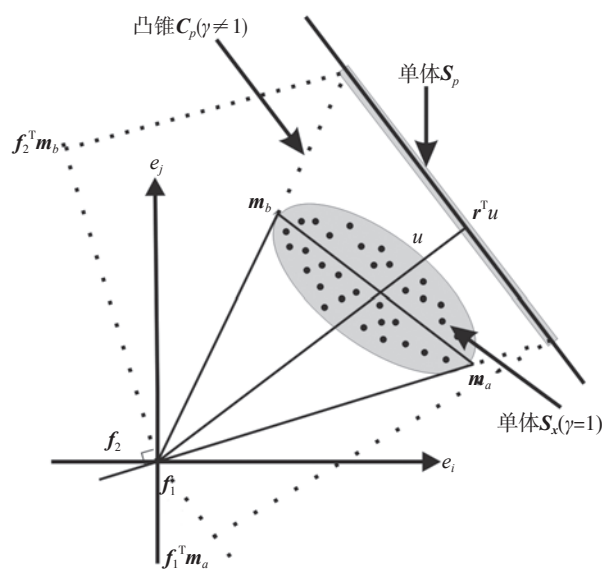
图3　VCA算法原理

在确定单体S_p后，VCA迭代地将数据投影到与之前已提取的端元构成的子空间正交的方向上，图3表示了VCA应用于单体S_p的两次迭代过程。在每一次迭代中，数据被投影到第一个方向f_1上，投影的极值对应于端元m_a，在下一次迭代中，端元m_b对应于将数据投影到f_2上的极值，f_2与m_a正交，该算法迭代执行直到确定数目的端元被提取出来。

Nascimento(2005，2006)对PPI、N-FINDR和VCA算法进行了比较，结果表明VCA算法提取的端元结果优于PPI、N-FINDR，尤其指出VCA算法的效率较高，在处理大数据量光谱数据时算法的速度更加明显。

2.3 SGA算法

SGA是N-FINDR算法的改进，它不是将使得单

体体积最大的所有顶点在同一高维空间提取出来，而是首先找出具有最大体积的两顶点单体，然后以此为基础，逐个找到使体积最大的顶点，直到找到最大体积的p个顶点。具体步骤如下：

（1）初始化：使用VD计算端元数p；

（2）随机产生一个目标像元，表示为t，遍历所有像元r，寻找满足产生最大行列式绝对值$\left|\det\begin{bmatrix}1 & 1\\ t & r\end{bmatrix}\right|$的像元作为第一个端元$A_1$，即：

$$A_1 = \arg\left\{\max_{r}\left[\left|\det\begin{bmatrix}1 & 1\\ t & r\end{bmatrix}\right|\right]\right\} \quad (5)$$

此过程需要利用PCA或者MNF变换将原始数据维数降为2，设置已获取端元数$n=1$；（第一个端元A_1取决于随机产生的目标像元t，Chang等人（2006）指出：A_1总是降维变换中第一主分量最大或者最小值所对应的像元，且总为最终的一个端元）；

（3）当$n\geq1$时，对于每一个像元，计算$V(A_1, A_2, \cdots, A_n, r)$，在计算之前应将原始数据维数$l$降为$n$；

$$V(A_1, A_2, \cdots A_n, r) = \frac{\left|\det\begin{bmatrix}1 & 1 & \cdots & 1 & 1\\ A_1 & A_2 & \cdots A_n & r\end{bmatrix}\right|}{n!} \quad (6)$$

（4）将$A_{n+1} = \arg\{\max_{r}[V(A_1, A_2, \cdots A_n, r)]\}$作为第$(n+1)$个端元；

（5）循环结束条件：如果$n<p$，则$n=n+1$，转到步骤（2），否则$(A_1, A_2, \cdots, A_p)$即为所要提取的端元集。

2.4　OSP算法

Harsanyi和Chang（1994）于1994年首次将正交子空间投影用于探测感兴趣目标，这个方法的优点在于通过信号光谱的逐步分离来提取出感兴趣的信号。起初，OSP需要端元的先验信息，后经学者们的改进（吴波等，2004；Chang，2003；Chang 等，2001），才用于端元的自动获取。

OSP用于端元提取的具体步骤如下：

（1）根据凸面几何学理论，利用最大光谱矢量法，即满足式（7），获取一个候选端元，它在影像中表现为亮度最大的像元。

$$d = \arg[\max_{x_i}(x_i^{\mathrm{T}}x_i)] \quad (7)$$

（2）判断候选端元是否为噪声，若是，剔除噪声，否则，为所需端元。

吴波等人（2004）设计了一种噪声判断方法：以候选端元为中心，在原图像上开一足够大的窗口，在该窗口中搜索与候选端元光谱相似度较高的像元，如果相似像元的数量大于给定阈值，则候选端元为所需的端元；否则，为噪声。

（3）消除已提取端元在光谱图像上的影响，生成新的光谱图像数据。

为了避免后续端元提取受已提取端元的影响，应在图像中消除已提取端元的影响。OSP消除已提取端元影响的思路如下：

将式（1）中的A分解为两部分，即$A=[D, U]$，其中$D=[d_1, d_2, \cdots, d_w]$表示已提取端元光谱矩阵（即感兴趣信息），$w$为已提取端元个数，$U$表示其余端元的光谱集合（即非感兴趣信息），同时把$s$也分解为相应的两部分，即$s=[s_D, s_U]^{\mathrm{T}}$，则式（1）变为：

$$x = Ds_D + Us_U + \varepsilon \quad (8)$$

D的正交投影矩阵P_D为：

$$P_D = I - D(D^{\mathrm{T}}D)^{-1}D^{\mathrm{T}} \quad (9)$$

式中，I为单位矩阵，则P_D为已知量，P_D作用于原高光谱图像（即左乘式（8））得到新的光谱图像：

$$P_D x = P_D Us_U \quad (10)$$

此时，新高光谱图像像元的光谱值$P_D Us_U$中不再包含已提取端元D的信息。

（4）判断是否满足结束条件（如已提取的端元达到指定数目等），如果满足，则结束运算，此时能够获得所有端元；如果不满足，则用新高光谱图像构成新凸面单体，循环操作（1）—（3）。

3　端元生成算法

3.1　ICE算法

ICE算法已申请专利，它将凸面几何模型与对模型中误差的合理估计、适当的统计步骤相结合，用于从高光谱影像中提取比MVT、N-FINDR等端元提取算法更多的细节信息（Berman 等，2003）。

ICE算法的目标是：

（1）不假定所有端元在图像上存在纯的像元；

（2）具有抗噪性；

（3）提供判断方法是否适合的评价标准，尤其是估计场景中存在的端元数目。

ICE算法的具体过程及原理如下（Berman 等，2003，2004）：

光谱解混可以通过最小化式（11）的余差平方和RSS（Residual Squared Sum）获取最优的端元、丰度。

$$\mathrm{RSS} = \sum_{i=1}^{N} (\boldsymbol{x}_i - \sum_{k=1}^{p} \boldsymbol{S}_{ik} \boldsymbol{A}_k)^{\mathrm{T}} (\boldsymbol{x}_i - \sum_{k=1}^{p} \boldsymbol{S}_{ik} \boldsymbol{A}_k) \quad (11)$$

ICE中使用RSS的另外一种形式：

$$\mathrm{RSS} = \sum_{j=1}^{d} (\boldsymbol{x}_j - S\boldsymbol{A}_j)^{\mathrm{T}} (\boldsymbol{x}_j - S\boldsymbol{A}_j) \quad (12)$$

式中，$\boldsymbol{x}_j$表示MNF变换后第j个波段的N个观察值组成的列向量，$\boldsymbol{A}_j$端元的p维列向量，$\boldsymbol{S}$表示p个端元对于N个像元的$N \times p$丰度矩阵，式(11)、(12)表明满足余差最小的端元集可以是由前$p-1$个MNF波段扩展而成的超平面内的p单体，它包含了投影到超平面上的数据点。

为了限制单体的大小，一般方法为增加一个与单体大小成比例的附加条件到式(11)、(12)中，ICE使用计算上更加简单的单体端元距离平方和SSD(Sum of Squared Distance)：

$$\mathrm{SSD} = \sum_{k=1}^{p-1} \sum_{l=k+1}^{p} (\boldsymbol{A}_k - \boldsymbol{A}_l)^{\mathrm{T}} (\boldsymbol{A}_k - \boldsymbol{A}_l) \quad (13)$$

经过推导，公式(13)可以写为：

$$\mathrm{SSD} = p(p-1)V \quad (14)$$

式中，V为单体端点方差之和。

ICE的目标函数为：

$$\mathrm{RSS}_{\mathrm{reg}} = (1-\mu)\mathrm{RSS}/N + \mu V \quad (15)$$

式中，μ为在(0，1)内较小的调整参数，式(15)需要根据p个端元和每个像元的p丰度进行最小化，一般采用迭代方式进行：给定端元估计，利用式(12)计算丰度矩阵$\boldsymbol{S}$，接着，利用丰度矩阵$\boldsymbol{S}$根据公式(16)计算每个$\boldsymbol{A}_j$：

$$\boldsymbol{A}_j = \left\{ \boldsymbol{S}^{\mathrm{T}} \boldsymbol{S} + \lambda (\boldsymbol{I}_M - 11^{\mathrm{T}}/p) \right\}^{-1} \boldsymbol{S}^{\mathrm{T}} \boldsymbol{x}_j \quad (16)$$

式中，$\lambda = N\mu/[(p-1)(1-\mu)]$，ICE将连续的$\mathrm{RSS}_{\mathrm{reg}}$的比值小于一定限差作为停止准则。

Berman(2003，2004)提出可以利用多次执行ICE算法来获取更为准确的端元个数和端元光谱，并利用ICE对Oatman地区的AVIRIS数据进行实验，取得了较好的实验结果。

3.2 MVC-NMF算法

MVC-NMF通过将体积限制加入到NMF中来将最小二乘分析和凸面几何结合起来。其提出的代价函数包括两部分，一部分估量观测数据与端元和丰度重建数据之间的近似误差，另一部分由最小体积限制组成。Miao和Qi(2007)把这两部分作为两种力：外力(最小化近似误差)使估计结果向点云外部移动，内力(最小化单体体积)在相反方向上使端元尽可能地相互靠近。算法具体过程为：

(1)利用VD估计端元数目p。

(2)构建目标函数

$$\begin{cases} \min f(\boldsymbol{A},\boldsymbol{S}) = \dfrac{1}{2} \| \boldsymbol{X} - \boldsymbol{A}\boldsymbol{S} \|_F^2 + \lambda J(\boldsymbol{A}) \\ \boldsymbol{A}_{i,j} \geqslant 0, \boldsymbol{S}_{i,j} \geqslant 0, 1_p^{\mathrm{T}} S = 1_n^{\mathrm{T}} \end{cases} \quad (17)$$

式中，1_p为元素全是1的p维列向量，1_n为元素全是1的n维列向量，$J(\boldsymbol{A})$为惩罚项，计算用估计的端元构成的单体体积，$\lambda \in \mathbf{R}$。

(3)初始化：从点云数据中随机选择p个点并将它们构成$\boldsymbol{A}$的初始值，$\boldsymbol{S}$矩阵也可以随机初始化，Miao和Qi(2007)在实验中，将矩阵$\boldsymbol{S}$初始化为零矩阵。

(4)停止准则：给定迭代次数和误差阈值。

(5)根据一定准则计算能够最小化目标函数的矩阵$\boldsymbol{A}$、$\boldsymbol{S}$，如果满足停止准则，则迭代停止，否则，更新矩阵$\boldsymbol{A}$、$\boldsymbol{S}$，继续寻找最小化目标函数的矩阵。

4 实验与分析

4.1 实验目的

文中利用高光谱模拟数据和真实高光谱图像对N-FINDR、VCA、SGA、OSP、ICE、MVC-NMF6种端元提取算法的结果进行比较和分析，具体实验包括：(1)端元数目不同时的实验对比；(2)对噪声的稳健性对比；(3)图像大小不同时的实验对比；(4)真实高光谱图像实验对比。

4.2 实验结果的相似性度量

为了评价实验的结果，文中采用Nascimento和Dias(2005)提出的光谱夹角距离(SAD，Spectral Angle Distance)、光谱信息散度(SID，Spectral Information Divergence)对6种端元提取算法进行了比较和评价。相似性测度公式如式(18)和式(19)所示，$\boldsymbol{a}$、$\hat{\boldsymbol{a}}$分别为真实光谱、估计光谱。式(13)中的$\boldsymbol{P} = \boldsymbol{a}/\sum_{i=1}^{l} \boldsymbol{a}_i$为光谱概率分布向量。

$$\mathrm{SAD} = \cos^{-1} \left(\frac{\boldsymbol{a}^{\mathrm{T}} \hat{\boldsymbol{a}}}{\|\boldsymbol{a}\| \cdot \|\hat{\boldsymbol{a}}\|} \right) \quad (18)$$

$$\begin{cases} \mathrm{SID} = D(\boldsymbol{a} \mid \hat{\boldsymbol{a}}) + D(\hat{\boldsymbol{a}} \mid \boldsymbol{a}) \\ D(\boldsymbol{a} \mid \hat{\boldsymbol{a}}) = \sum_{i=1}^{l} p_i \log \left(\dfrac{p_i}{\hat{p}_i} \right) \\ \boldsymbol{P} = \boldsymbol{a}/\sum_{i=1}^{l} \boldsymbol{a}_i \end{cases} \quad (19)$$

4.3　实验数据描述

本文利用USGS地物光谱库(Clark 等，2007)中的光谱集来构建模拟数据，该数据库的光谱数据包含224个光谱波段(实验仅使用了188个波段)，光谱覆盖范围为0.38—2.5 μm、光谱分辨率为10 nm。文中随机选取光谱库中k条光谱构建大小为size×size(实验中采用的大小为64×64、81×81和100×100)的模拟数据，模拟数据中每个像元的丰度向量随机产生(满足非负与和为一限制条件)，并且将丰度向量中存在元素大于0.8的像元光谱替换为所用到的k条光谱的平均值(消除数据中的纯像元)，实验为模拟数据中添加了均值为零的高斯噪声。

真实数据为AVIRIS于1995年7月获取的Nevada州Cuprite采矿区的数据。该高光谱数据大小为100×100，拥有224个波段(0.4—2.5 μm)，空间分辨率和光谱分辨率分别为20 m和10 nm。实验中使用了188个波段，波段1—2，104—113，148—167，221—224由于存在水蒸气吸收和信噪比较低而被去除。利用ATREM(Atmospheric Removal)(Gao和Goetz，1990)方法将该数据纠正为反射光谱数据之后，残余噪声使用EFFORT(Empirical Flat Field Optimized Reflectance Transform)(Boardman，1998)方法实现最小化。实验数据的假彩色图像(R：波段7，G：波段32，B：波段62)如图4所示：
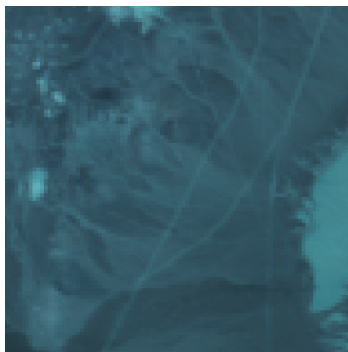
图4　Cuprite地区实验数据图像

4.4　实验结果与分析

实验中ICE*、MVC-NMF算法的最大迭代次数均为150次，参数λ=0.05，且两种方法均使用VCA和全限制最小二乘方法(FCLS，Fully Constrained Least Squares)(Heiz和Chang，2001)对端元及丰度进行初始

化，实验中表格内统计的SAD单位均为度。实验所用的计算机主频为2.68 GHz，内存1 G，端元提取算法均采用Matlab 7.0平台进行实现。

4.4.1　端元数不同时的实验对比

该实验的目的为对比在不同端元数目情况下6种端元提取算法的结果，实验中模拟图像大小为64×64，添加SNR=30 db的高斯噪声。表1、2分别为在端元数为4、5、6、7时6种算法端元提取结果的相似性测度及运行时间，图5为模拟数据、真实端元、6种算法提取的端元在二维坐标系下的投影(PCA变换)。从表1、图5可以看出，六种端元提取算法的精度由高到低依次为：MVC-NMF、ICE、VCA、OSP、N-FINDR和SGA，从实验运行时间可以看出，在端元数不同的情况下，6种端元提取算法效率由高到低依次为：OSP、VCA、SGA、N-FINDR、MVC-NMF和ICE。

4.4.2　对噪声的稳健性对比

为了验证6种端元提取算法的抗噪性，利用光谱库中的4条光谱构建大小为64×64的模拟图像，并在模拟数据中分别添加SNR=20 db、30 db、40 db和50 db的高斯噪声。表3、4分别列出了在不同的信噪比下6种算法获取端元光谱的相似性测度和运行时间，图6、7分别为信噪比为20 db和40 db的情况下，6种方法获取的端元光谱曲线。从表3、图6、7可以看出：信噪比减小的情况下，6种方法的结果都逐渐变差，且6种端元提取算法对噪声的鲁棒性由高到低依次为：MVC-NMF、ICE、VCA、OSP、N-FINDR和SGA，从实验运行时间可以看出，在信噪比不同的情况下，6种端元提取算法效率由高到低依次为：OSP、VCA、SGA、N-FINDR、MVC-NMF和ICE。

4.4.3　图像大小不同时的实验对比

该实验的目的是对比在图像大小不同时6种端元提取算法的结果，实验利用USGS地物光谱库中4条光谱构建模拟图像，并为模拟图像添加SNR=30 db的高斯噪声。表5、6分别为在图像大小为64×64、81×81、100×100时6种算法端元提取结果的相似性测度及运行时间。从表5可以看出，6种端元提取算法的精度由高到低依次为：MVC-NMF、ICE、VCA、OSP、N-FINDR和SGA，从实验运行时间可以看出，在图像大小不同的情况下，6种端元提取算法效率

*Berman（2009）提出仅保留凸包中重要点以提高ICE算法效率的方法，该方法也同样可以应用于其他5种方法，文中实验中ICE与其他算法均没有采用该方法。

由高到低依次为：OSP、VCA、SGA、N-FINDR、MVC-NMF和ICE。

4.4.4 真实高光谱图像实验对比

利用VD方法确定4.2节中介绍的Cuprite地区AVIRIS高光谱图像端元数目为9，端元提取的结果可以采用USGS地面光谱库数据进行比较(Winter，1999a；Nascimento，2006；Berman 等，2003；Miao和Qi，2007)，6种端元提取算法进行端元提取的结果如表7所示，从表7可以看出，6种端元提取算法应用于真实高光谱图像时的精度由高到低依次为：MVC-NMF、ICE、N-FINDR、VCA、SGA和OSP，从表8实验运行时间可以看出，6种端元提取算法效率由高到低依次为：OSP、VCA、SGA、N-FINDR、MVC-NMF和ICE。

真实高光谱图像的实验结果与模拟数据实验结果略有不同，即VCA算法提取的结果精度略低于N-FINDR算法，但这与Nascimento(2006)实验结果的结论仍然具有一致性：VCA与N-FINDR的算法精度相当或略优于N-FINDR，但效率上的优势更加明显。

通过实验可以发现：端元识别算法效率比较高，但精度低于端元生成算法，这是因为EIA算法从高光谱数据中寻找最具有代表性的像元光谱作为端元，而EGA需要根据现有高光谱数据依据一定的优化准则去计算端元，实验比较的结果与EIA、EGA算法理论上的优缺点分析具有一致性。

表1　端元数不同时的实验对比

端元数	N-FINDR		VCA		SGA		OSP		ICE		MVC-NMF	
	SAD	SID	SAD	SID	SAD	SID	SAD	SID	SAD	SID	SAD	SID
4	3.908	0.013	3.293	0.011	7.483	0.053	3.908	0.013	5.273	0.033	2.409	0.005
5	12.142	0.066	11.434	0.062	16.111	0.161	13.778	0.079	9.747	0.031	5.450	0.032
6	9.674	0.066	9.235	0.039	13.466	0.111	7.945	0.033	5.308	0.023	1.614	0.002
7	11.034	0.097	11.769	0.089	9.009	0.066	10.881	0.096	6.452	0.033	3.022	0.008

表2　端元数不同时算法的运行时间

端元数	程序运行时间/s					
	N-FINDR	VCA	SGA	OSP	ICE	MVC-NMF
4	4.9	0.5	0.9	0.4	542.2	110.4
5	4.8	0.5	0.9	0.5	689.9	120.7
6	5.0	0.5	1.1	0.4	824	174.4
7	5.3	0.5	1.1	0.6	941	273.5
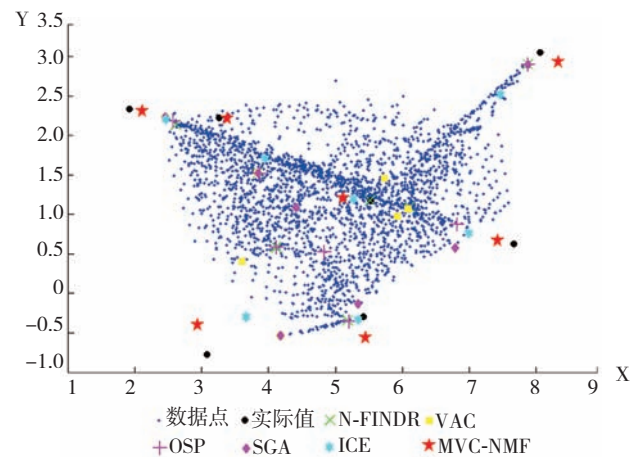
图5　端元数为7时端元提取结果的二维投影图

表3　对噪声的稳健性对比

信噪比/db	N-FINDR		VCA		SGA		OSP		ICE		MVC-NMF	
	SAD	SID	SAD	SID	SAD	SID	SAD	SID	SAD	SID	SAD	SID
20	7.379	0.037	3.265	0.012	10.996	0.081	7.349	0.035	3.054	0.013	1.019	0.0009
30	3.908	0.013	3.293	0.011	7.483	0.053	3.908	0.013	3.073	0.010	2.409	0.005
40	2.621	0.005	2.808	0.005	4.411	0.011	2.589	0.005	2.071	0.004	0.575	0.0004
50	2.910	0.006	3.651	0.012	2.907	0.006	2.697	0.006	2.403	0.010	0.422	0.0001

表4   添加噪声信噪比不同时算法的运行时间

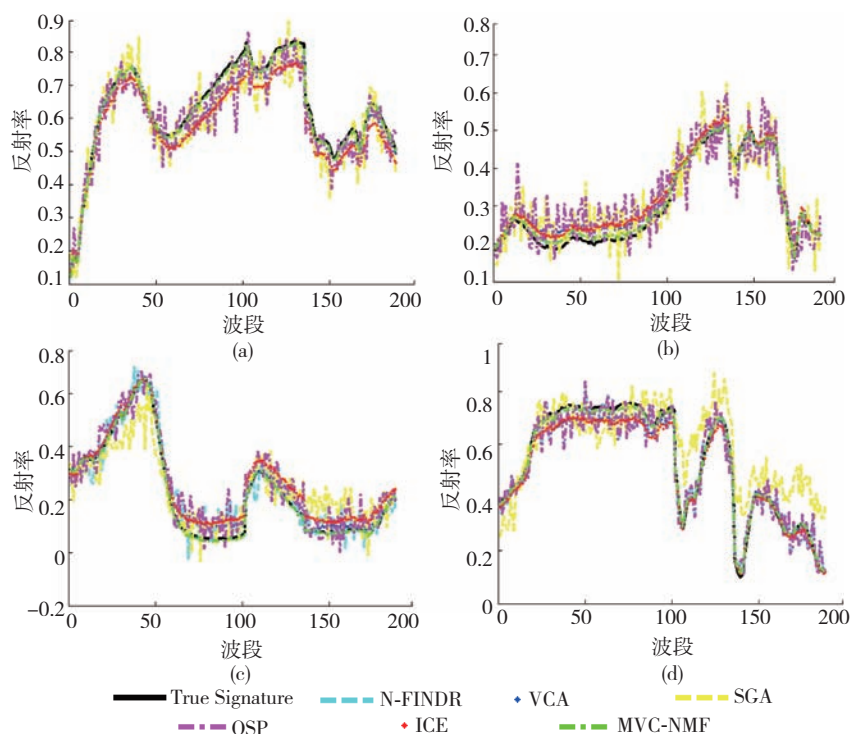| 信噪比/db	程序运行时间/s					
	N-FINDR	VCA	SGA	OSP	ICE	MVC-NMF
20	5.1	0.5	0.8	0.4	563.4	120.1
30	4.9	0.5	0.9	0.4	542.2	110.4
40	4.8	0.9	0.8	0.4	541.6	117.5
50	6.3	0.6	0.8	0.4	588.5	126.1

图6   信噪比为20 db时的端元提取结果

(a)端元1；(b)端元2；(c)端元3；(d)端元4
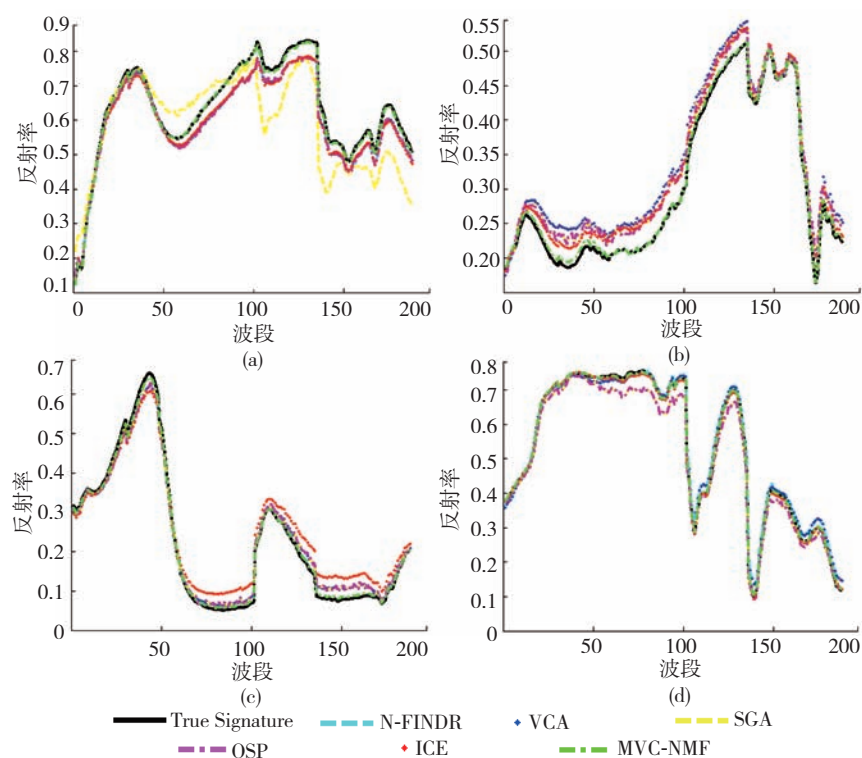
图7   信噪比为40 db时的端元提取结果

(a)端元1；(b)端元2；(c)端元3；(d)端元4

表5 图像大小不同时的实验对比

图像大小/像元	N-FINDR		VCA		SGA		OSP		ICE		MVC-NMF	
	SAD	SID	SAD	SID	SAD	SID	SAD	SID	SAD	SID	SAD	SID
64×64	3.908	0.013	3.293	0.011	7.483	0.053	3.908	0.013	3.273	0.012	2.409	0.005
81×81	2.511	0.005	1.286	0.001	2.632	0.006	2.526	0.005	1.147	0.001	0.347	0.0001
100×100	2.136	0.003	0.992	0.001	2.194	0.003	2.101	0.003	0.874	0.001	0.279	0.0001

表6 图像大小不同时算法的运行时间

图像大小/像元	程序运行时间/s					
	N-FINDR	VCA	SGA	OSP	ICE	MVC-NMF
64×64	4.9	0.5	0.9	0.4	542.2	110.4
81×81	8.3	0.7	1.1	0.5	719	137.7
100×100	12.4	0.8	1.4	0.9	902	347

表7 真实高光谱图像实验对比

图像大小/像元	N-FINDR		VCA		SGA		OSP		ICE		MVC-NMF	
	SAD	SID	SAD	SID	SAD	SID	SAD	SID	SAD	SID	SAD	SID
100×100	6.192	0.021	6.491	0.023	6.991	0.028	8.080	0.031	5.623	0.019	5.025	0.012

表8 处理Cuprite地区高光谱图像时算法的运行时间

图像大小/像元	程序运行时间/s					
	N-FINDR	VCA	SGA	OSP	ICE	MVC-NMF
100×100	13.1	0.9	1.5	0.9	909	354

5 结 论

混合像元问题的解决有助于实现高精度分类和子像元目标识别，为更加充分地利用高光谱图像提供了技术支撑。本文通过分析现有的经典端元提取算法，将端元提取算法分为：端元识别算法和端元生成算法，对目前较为常用的6种端元提取算法进行了算法的总结和实验，通过研究可以得出以下结论：

(1)从端元提取结果的精度上考虑，端元生成算法优于端元识别算法提取的端元结果，MVC-NMF算法端元提取的结果精度最高，SGA算法虽然为N-FINDR算法的改进，但端元提取的结果精度有所降低；

(2)从运算效率上考虑，端元识别算法优于端元生成算法，尤其是VCA和OSP算法。SGA算法作为N-FINDR算法的改进，效率上有较大的提高。

无论是哪类端元提取算法，都会有其自身的不足，要想获得更好的混合像元分解结果仅仅考虑一类算法是不够的，根据实际应用及算法各自的优缺点，对端元提取算法的下一步研究提出以下展望：

(1)如果实际应用更注重效率，则可以选择EIA算法进行端元提取，尤其是VCA、OSP算法精度上相对比较高的同时，效率上的优势更加明显；如果实际应用对混合像元分解的精度要求比较高，应该选择EGA算法进行端元提取，相比较ICE算法而言可以选择MVC-NMF算法进行混合像元分解；

(2)可以将端元识别算法结果作为端元生成算法的初始值，加快算法的收敛，如VCA算法效率很高且端元提取的结果略优于其他端元识别算法，可以将VCA算法结果作为ICE和MVC-NMF算法的端元初始值，以利于加快EGA算法的迭代收敛以及提高端元提取算法的效率和结果的可靠性；

(3)在混合像元分解前，可以利用端元识别算法先提取端元，然后去除位于初始端元构成的凸面单体内部的点(判断利用非限制性最小二乘计算的丰度是否满足非负以及和为1的约束条件)，仅利用端元生成算法处理位于初始端元构成的凸包外部的点，这样可以进一步提高算法的效率和端元提取结果的可靠性。

志　谢　感谢MVC-NMF算法作者Qi Hairong教授提供的MVC-NMF算法源码程序，以及ICE算法作者Berman教授在ICE算法上的指导。

REFERENCES

Berman M, Kiiveri H, Lagerstrom R, Ernst A, Dunne R and Huntington J F. 2003. ICE: an automated statistical approach to identifying endmembers in hyperspectral images. IEEE International Geoscience and Remote Sensing Symposium, France: Toulouse, **1**: 279–283

Berman M, Kiiveri H, Lagerstrom R, Ernst A, Dunne R and Huntington J F. 2004. ICE: a statistical approach to identifying endmembers in hyperspectral images. *IEEE Transactions on Geoscience and Remote Sensing*, **42**(10): 2085–2095

Berman M, Phatak A, Lagerstrom R and Wood B R. 2009. ICE: a new method for the multivariate curve resolution of hyperspectral images. *Journal of Chemometrics*, **23**(2): 101–116

Boardman J W. 1998. Post-ATREM polishing of AVIRIS apparent reflectance data using EFFORT: a lesson in accuracy versus precision. Summaries of the Seventh JPL Airborne Earth Science Workshop. Pasadena: JPL Publication

Boardman J W, Kruse F A and Green R O. 1995. Mapping target signatures via partial unmixing of AVIRIS data: in Summaries. Fifth JPL Airborne Earth Science Workshop. Pasadena: JPL Publication: 23–26

Bowles J H, Palmadesso P J, Antoniades J A, Baumbeck M M and Rickard L J. 1995. Use of filter vectors in hyperspectral data analysis. Infrared Spaceborne Remote Sensing III, SPIE Proceedings. San Diego, USA, **2553**: 148–157

Chang C I. 2003. Hyperspectral Imaging: Techniques for Spectral Detection and Classification. New York: Kluwer Academic/Plenum Publishers: 40–41

Chang C I, Du Q, Chiang S S, Heinz D C and Ginsberg I W. 2001. Unsupervised target subpixel detection in hyperspectral imagery. Conference Algorithms for Multispectral, Hyperspectral, and Ultraspectral Imagery VII, SPIE Proceedings. Orlando FL, USA, **4381**: 370–379

Chang C I, Wu C C, Liu W M and Ouyang Y C. 2006. A new growing method for simplex-based endmember extraction algorithm. *IEEE Transactions on Geoscience and Remote Sensing*, **44**(10): 2804–2819

Clark R N, Swayze G A, Wise R, Livo K E, Hoefen T M, Kokaly R F

and Sutley S J. 2007. splib06b. USGS Digital Spectral Library. [2009-11-3]. http://speclab.cr.usgs.gov/spectrallib.html

Craig M D. 1994. Minimum-volume transforms for remotely sensed data. *IEEE Transactions on Geoscience and Remote Sensing*, **32**(3): 542–552

Gao B C and Goetz A F H. 1990. Column atmospheric water vapor and vegetation liquid water retrievals from airborne imaging spectrometer data. *Journal of Geophysical Research*, **95**(D4): 3549–3564

Gruninger J H, Ratkowski A J and Hoke M L. 2004. The sequential maximum angle convex cone (SMACC) endmember model. Algorithms for Multispectral, Hyperspectral and Ultraspectral Imagery X, SPIE Proceedings. Orlando, USA, **5425**: 1–14

Harsanyi J C and Chang C I. 1994. Hyperspectral image classification and dimensionality reduction: an orthogonal subspace projection approach. *IEEE Transactions on Geoscience and Remote Sensing*, **32**(4): 779–785

Heinz D C and Chang C I. 2001. Fully constrained least squares linear spectral mixture analysis method for material quantification in hyperspectral imagery. *IEEE Transactions on Geoscience and Remote Sensing*, **39**(3): 529–545

Ifarraguerri A and Chang C I. 1999. Multispectral and hyperspectral image anlysis with convex cones. *IEEE Transactions on Geoscience and Remote Sensing*, **37**(2): 756–770

Kumar A and Min H A. 2008. Some issues related with sub-pixel classification using Hyperion data. ISPRS XXI VII, Beijing: ISPRS

Miao L D and Qi H R. 2007. Endmember extraction from highly mixed data using minimum volume constrained nonnegative matrix factorization. *IEEE Transactions on Geoscience and Remote Sensing*, **45**(3): 765–777

Nascimento J M P. 2006. Supervised Hyperspectral Unmixing. Lisboa: Universidade Técnico de Lisboa: 47–72

Nascimento J M P and Dias J M B. 2005. Vertex component analysis: a fast algorithm to unmix hyperspectral data. *IEEE Transactions on Geoscience and Remote Sensing*, **43**(4):898–910

Neville R A, Staenz K, Szeredi T, Lefebvre J and Hauff P. 1999. Automatic endmember extraction from hyperspectral data for mineral exploration. Proceedings of Fourth International Airborne Remote Sensing Conference and Exhibition/21st Canadian Symposium on Remote Sensing. Ottawa, Canada: 21–24

Plaza A and Chang C I. 2005. An improved N-FINDR algorithm in implementation. Algorithms and Technologies for Multispectral, Hyperspectral and Untraspectral Imagery XI, SPIE Proceedings. Orlando, USA, **5806**: 298–306

Plaza A and Chang C I. 2006. Impact of initialization on design of endmember extraction algorithms. *IEEE Transactions on Geoscience and Remote Sensing*, **44**(11): 3397–3407

Winter M E. 1999a. N-FINDR: an algorithm for fast autonomous spectral end-member determination in hyperspectral data. Imaging Spectrometry V, SPIE Proceedings. Denver CO, USA, 3753: 266–275

Winter M E. 1999b. Fast autonomous spectral end-member determination In hyperspectral data. Proceedings of the Thirteenth International Conference on Applied Geologic Remote Sensing. Vancouver, B C, Canada: 337–344

Winter M E. 2004. A proof of the N-FINDR algorithm for the automated detection of end-members in a hysperspectral image // Algorithms and Technologies for Multispectral, Hyperspectral, and Ultraspectral Imagery X, SPIE Proceedings. Orlando, USA: 12–15

Wu B, Zhang L P and Li P X. 2004. Unsupervised orthogonal subspace projection approach to unmix hyperspectral imagery automatically. *Journal of Image and Graphics*, **9**(11): 1392–1396

Zhang J K, Rivard B and Rogge D M. 2008. The successive projection algorithm (SPA), an algorithm with a spatial constraint for the automatic search of endmembers in hyperspectral data. Sensors, **8**: 1321–1342

Zhang X, Tong X H and Liu M L. 2009. An improved N-FINDR algorithm for endmember extraction in hyperspectral imagery. Urban Remote Sensing Joint Event. Shanghai, China

附中文参考文献

吴波，张良培，李平湘. 2004. 非监督正交子空间投影的高光谱混合像元自动分解. 中国图象图形学报，**9**(11): 1392–1396